Nano Research

**Open Access**

**Research Article**

# Hollow cobalt disulfide/nitrogen-doped carbon nanoboxes for high stability sodium-ion battery anodes

Shijian Xiu[1], Na Liu[1], Huiyeong Kang[2], Woo Suk Baek[2], So Hee Kim[2], Aihua Jin[1,3], Seung-Ho Yu[3], and Bo Quan[1,4]

[1] *Key Laboratory of Electrochemical Energy Storage Materials of Jilin Province, Department of Chemistry, Yanbian University, Yanji 133002, China*
[2] *Advanced Analysis Center, Korea Institute of Science and Technology, Seoul 02792, Republic of Korea*
[3] *Department of Chemical and Biological Engineering, Korea University, 145 Anam-ro, Seongbuk-gu, Seoul 02841, Republic of Korea*
[4] *Analysis and Testing Center, Yanbian University, Yanji 133002, China*

**Cite this article:** *Nano Research*, **2025**, *18*, 94907800. https://doi.org/10.26599/NR.2025.94907800

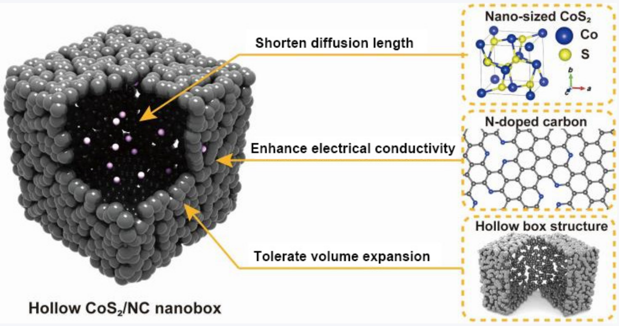

**ABSTRACT:** Metal sulfides have attracted significant attention in sodium-ion battery research owing to their high theoretical capacity. However, their practical application is hindered by volume fluctuations and low conductivity caused by conversion reactions. In this study, hollow cobalt disulfide/nitrogen-doped carbon ($CoS_2$/NC) nanoboxes were synthesized from cobalt-based Prussian blue analogues (PBA) through a sulfidation process. The resulting nanoboxes, approximately 500 nm in size, possess hollow interiors constructed from interconnected primary nanoparticles (~ 50 nm). The unique hierarchical structure provides abundant void space to accommodate volume changes and shortens transport pathways. Furthermore, the integration of nitrogen-doped carbon matrix significantly enhances the electronic conductivity. When employed as an anode material for sodium-ion batteries, hollow $CoS_2$/NC nanoboxes delivered an outstanding desodiation capacity of 619.4 mAh·g$^{-1}$ at 5 A·g$^{-1}$ over 400 cycles with an average capacity loss of only 0.04% per cycle. This study highlights the potential of PBAs as precursors for synthesizing nanoscale metal sulfides with nitrogen-doped carbon matrices, offering a promising approach to enhance electrochemical performance in energy storage systems.

**KEYWORDS:** cobalt disulfides, Prussian blue analogues, hollow structure, anode materials, sodium-ion batteries

## 1 Introduction

Sodium-ion batteries (SIBs) have garnered significant interest in recent years due to the natural abundance, low cost, and environmental advantages of sodium [1–3]. While sodium shares similar chemical properties with lithium, allowing SIBs to benefit from advances in lithium-ion battery (LIB) technology. However, key differences between SIBs and LIBs pose challenges. The larger sodium ionic radius (1.02 Å) and the lower electrochemical potential (–2.71 V vs. standard hydrogen electrode (SHE)) reduce diffusion kinetics and increase migration barriers, hindering efficient sodium-ion transport [2, 4, 5]. Consequently, the development of advanced electrode materials to overcome these limitations is essential for achieving high performance and long-term cycling stability in SIBs [6–8].

Cobalt disulfide ($CoS_2$) has emerged as a promising candidate for SIBs due to its high theoretical capacity of 872 mAh·g$^{-1}$ [9]. However, its practical application is hindered by low conductivity, severe volume expansion, and the polysulfide shuttle effect, which arise from reaction barriers [10, 11]. To overcome these drawbacks, various strategies, such as nanoscale material design, defect engineering, and heterostructure formation, have been employed [12–16]. These strategies are often used in combination for enhanced effectiveness. For example, nitrogen-doped carbon-coated Co nanoparticles (Co@NC/CNT, CNT refers to carbon nanotube) were synthesized using a zeolitic imidazolate framework-67 (ZIF-67) core–shell structure with an outer ZIF-8 layer. Ion exchange with Sb and subsequent high-temperature sulfidation

---

**Received:** April 4, 2025; **Revised:** June 26, 2025
**Accepted:** July 14, 2025

✉Address correspondence to Aihua Jin, jinaihua@ybu.edu.cn; Seung-Ho Yu, seunghoyu@korea.ac.kr; Bo Quan, quanbo@ybu.edu.cn

produced $CoS_2/Sb_2S_3$@NC/CN heterostructures, which delivered a reversible capacity of 360.1 mAh·g$^{-1}$ at 0.5 A·g$^{-1}$ after 200 cycles [17]. Similarly, metal–organic framework (MOF)-derived $CoS_2$/N-doped carbon grown on $Ti_3C_2T_x$ MXene hollow spheres (MXene@$CoS_2$/NC) were synthesized by Li et al. The combination of MXene hollow spheres and MOF-derived nitrogen-doped carbon effectively mitigated $CoS_2$ volume expansion and showed improved electrochemical stability with a high reversible capacity of 620 mAh·g$^{-1}$ at 0.2 A·g$^{-1}$ [18].

Prussian blue analogues (PBA), as one of the MOF materials, are valued for their open frameworks, abundant redox sites, and stable porous structures [19–21]. These properties enable the formation of uniformly distributed metal or metal compound nanoparticles while minimizing agglomeration. PBAs also contribute to nitrogen doping, which enhances the conductivity [22, 23]. Thus, PBAs are widely used as precursors for battery electrode materials. Chen et al. developed a carbon-coated cobalt-iron sulfide composite (PBC1-1S) from CoFe PBA precursors. As an anode material for SIBs, PBC1-1S exhibited a reversible capacity of 500 mAh·g$^{-1}$ at 50 mA·g$^{-1}$ [24]. Similarly, CuFe PBA was converted into a heterostructured composite of CuS/$FeS_2$ embedded in NC (CuS/$FeS_2$@NC) via carbonization and sulfidation. The resulting CuS/$FeS_2$@NC nanocubes exhibited a sodiation capacity of 537 mAh·g$^{-1}$ at 5 A·g$^{-1}$ over 300 cycles with 99.1% capacity retention [25].

Building on these advancements, hollow $CoS_2$/NC nanoboxes were synthesized using Co-based PBAs as precursors. A straightforward self-assembly approach followed by sulfidation was employed, with sulfur (S) powder serving as the sulfur source. The resulting hollow nanoboxes exhibited approximately 500 nm in size and were composed of ~ 50 nm $CoS_2$ nanoparticles. The hollow $CoS_2$/NC nanoboxes achieved an impressive capacity of 771.2 mAh·g$^{-1}$ at a current density of 0.5 A·g$^{-1}$ and maintained 627.7 mAh·g$^{-1}$ after 100 cycles. Additionally, they also delivered excellent rate performance of 619.4 mAh·g$^{-1}$ at 5 A·g$^{-1}$ over 400 cycles, with an average capacity attenuation of just 0.04% per cycle. This superior performance is attributed to the interconnected nanoparticles and internal void spaces in the nanoboxes. This unique architecture could facilitate efficient ion and electron transport while buffering the volume changes. The nitrogen-doped carbon matrix further enhances electrical conductivity and overall structural integrity.

## 2 Experimental

### 2.1 Chemicals and materials

Potassium hexacyanocobaltate ($K_3[Co(CN)_6]$, 98.0%) and $CoS_2$ (99.9%) were purchased from Aladdin Ltd. Cobalt acetate tetrahydrate ($Co(OAc)_2 \cdot 4H_2O$, 99.0%, OAc stands for acetate) was sourced from Alfa Aesar. Sodium citrate ($C_6H_5Na_3O_7$, 99.0%) was purchased from Sigma Aldrich. Sulfur powder (99.5%) was purchased from Thermo Scientific. All reagents were of analytical grade and used without further purification unless otherwise specified.

### 2.2 Preparation of Co PBAs

Co PBAs were synthesized using a classical coprecipitation method. Initially, $K_3[Co(CN)_6]$ (4 mmol, 1.3293 g) was dissolved in 100 mL deionized water to prepare Solution A. $Co(OAc)_2 \cdot 4H_2O$ (6 mmol, 1.4945 g) and $C_6H_5Na_3O_7$ (9 mmol, 2.6469 g) were dissolved in 100 mL deionized water to form Solution B. Under vigorous stirring, Solution A was slowly dripped into Solution B, triggering the coprecipitation reaction. The resulting mixture was stirred for 20 min and then aged for 24 h. The precipitate was collected by centrifugation, washed three times with deionized water, and finally vacuum-dried at 60 °C for 12 h.

### 2.3 Preparation of hollow $CoS_2$/NC nanoboxes

Co PBAs (0.3 g) and sulfur powder (0.3 g) were uniformly mixed and pulverized to ensure uniformity. The mixture was transferred to a porcelain boat and subjected to vulcanization in an inert argon atmosphere. The procedure involved pre-vulcanization at 155 °C for 5 h, followed by a gradual temperature increase to 500 °C at a controlled heating rate of 3 °C·min$^{-1}$ over 2 h. After cooling to room temperature, hollow $CoS_2$/NC nanoboxes were successfully obtained.

### 2.4 Preparation of ball-milled $CoS_2$ ($CoS_2$/BM)

For comparison, 1 g $CoS_2$ was ground using a high-energy ball mill. The milling process involved 10 cycles of 15 min of grinding at 500 rpm, alternated with 15 min of rest. The finely $CoS_2$/BM was collected for further analysis.

### 2.5 Material characterization

The morphology of $CoS_2$/NC was examined by scanning electron microscopy (SEM, JEOL JSM-IT700HR/LA) and transmission electron microscopy (TEM, Thermo Fisher Talos F200X). Powder X-ray diffraction (XRD) was conducted on a Rigaku Dmax-2200/pc X-ray diffractometer. Raman spectra were performed on a Horiba Lab RAM HR Evolution Raman spectrometer with a 532 nm laser. Inductively coupled plasma-mass spectroscopy (ICP-MS) was conducted by Agilent 5110. Surface chemistry was analyzed using X-ray photoelectron spectroscopy (XPS, Thermo Scientific) with Al K$\alpha$ radiation. Thermogravimetric analysis (TGA) was performed on a Mettler Toledo TGA2 at a temperature range of 35–1000 °C. The specific surface area and pore information were evaluated with a Micromeritics ASAP 2460 analyzer, with calculations based on Brunauer–Emmett–Teller (BET) method and the density functional theory (DFT) methods.

### 2.6 Electrochemical characterization

Electrochemical performance was evaluated using CR2032 type coin cell. The electrode slurry consisted of active materials, Super P conductive carbon, and polyacrylic acid (PAA) binder in n-methyl-2-pyrrolidone (NMP) at a mass ratio of 70:15:15. The slurry was coated on copper foil collector and dried under vacuum at 120 °C for 12 h. The loading mass of active materials was ~ 1.7 mg·cm$^{-2}$ with a diameter of 12 mm. Coin cells were assembled in an Ar-filled glove box, utilizing a 16 mm sodium metal as cathode, and Whatman GF/C as the separator. The electrolyte consisted of 1 M $NaPF_6$ dissolved in diglyme. Galvanostatic charge–discharge cycling was performed in WBCS3000 cycler system. Electrochemical impedance spectroscopy (EIS) was conducted on an Autolab PGSTAT302N electrochemical workstation over a frequency range from 0.01 to 100 kHz. The conductivity measurements were tested by ST2558B-F02 probe in conjunction with the ST2253A four-probe tester.

## 3 Results and discussion

### 3.1 Structural characterization

Hollow $CoS_2$/NC nanoboxes were synthesized through a sequential co-precipitation and sulfidation process, as illustrated in Fig. 1(a). Initially, Co PBAs were formed via spontaneous bridging interactions between $Co^{2+}$ ions and $[Co(CN)_6]^{3-}$ octahedral complexes. Sodium citrate, serving as a coordinating inhibitor, competed with $[Co(CN)_6]^{3-}$ to modulate the coordination kinetics. This regulation facilitated the controlled synthesis of nanocube-shaped Co PBAs [26, 27]. Subsequently, sulfidation using sulfur powder converted the Co PBAs nanocubes into hollow $CoS_2$/NC nanoboxes.

The morphology of these materials was characterized by SEM and TEM. As shown in Figs. 1(b) and 1(c) and Fig. S1 in the Electronic Supplementary Material (ESM), Co PBAs exhibit a heterogeneous cubic structure with particle sizes of approximately 500 nm. After the sulfidation process, Co PBAs underwent a significant morphological transformation into hollow nanoboxes, while largely retaining their original size. These nanoboxes are composed of $CoS_2$ nanoparticles with an average diameter of ~ 50 nm (Figs. 1(d)–1(g) and Fig. S2 in the ESM). As observed in Figs. S2(c) and S2(f) in the ESM, the walls are formed by one or two layers of $CoS_2$ nanoparticles, yielding a wall thickness of around 100 nm. This structural evolution highlights the complexity and effectiveness of the sulfidation process in generating hollow architectures. In Fig. 1(g) and 1(i), the high-resolution TEM (HR-TEM) images showed that hollow $CoS_2$/NC nanoboxes exhibit an interlayer spacing of 0.246 nm, corresponding to the (210) crystal plane of $CoS_2$. High-angle annular dark-field scanning TEM (HAADF-STEM) and energy-dispersive spectroscopy (EDS) images confirmed the formation of the hollow $CoS_2$ structure and uniform nitrogen distribution within the nanobox-shaped carbon matrix (Fig. 1(j)). For comparison, high energy ball-milling method was used to prepare small-sized $CoS_2$/BM. As shown in Fig. S3 in the ESM, this simple process reduced the grain size of bare $CoS_2$ to a non-uniform distribution ranging from 50 to 500 nm.

XRD analysis monitored the structural evolution of the prepared products (Fig. S4 in the ESM and Fig. 2(a)). The diffraction peaks of Co PBAs matched well with $Co_3(Co(CN)_6)_2$ (PDF No. 77-1161) [28, 29]. Upon sulfidation at 500 °C, hollow $CoS_2$/NC nanoboxes exhibited six distinct peaks at 27.9°, 32.3°, 36.2°, 39.8°, 46.3°, and 54.9°, corresponding to the (111), (200), (210), (211), (220), and (311) planes of cubic $CoS_2$ (PDF No. 41-1471), respectively, indicating high phase purity and the absence of impurities (Fig. 2(a)) [30–32]. The XRD pattern of $CoS_2$/BM was identical to that of hollow $CoS_2$/NC nanoboxes.

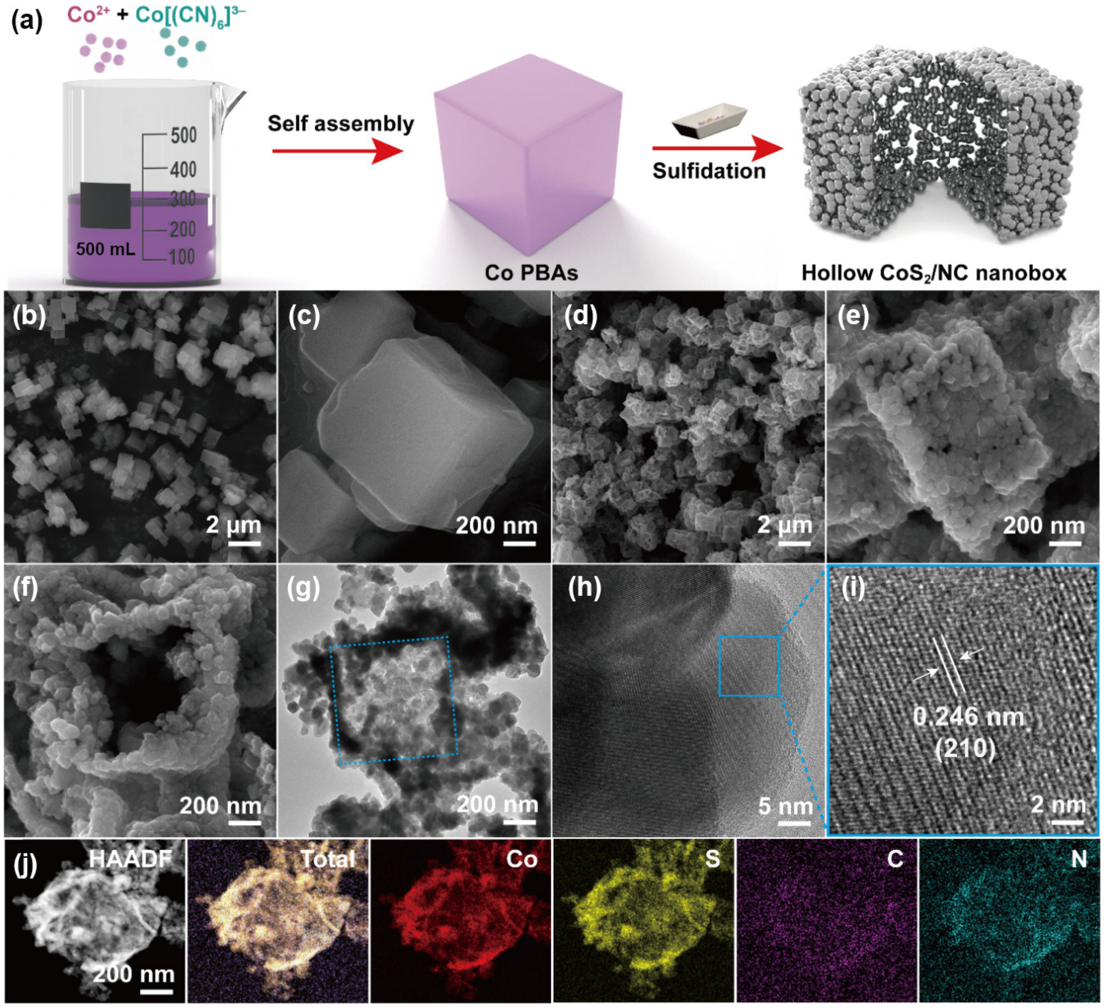

**Figure 1** (a) Schematic illustration depicting the fabrication of $CoS_2$/NC. ((b)–(f)) SEM images of ((b) and (c)) Co PBAs and ((d)–(f)) hollow $CoS_2$/NC nanoboxes. ((g)–(i)) HR-TEM images and (j) HAADF-STEM image and corresponding EDS mappings of hollow $CoS_2$/NC nanoboxes.

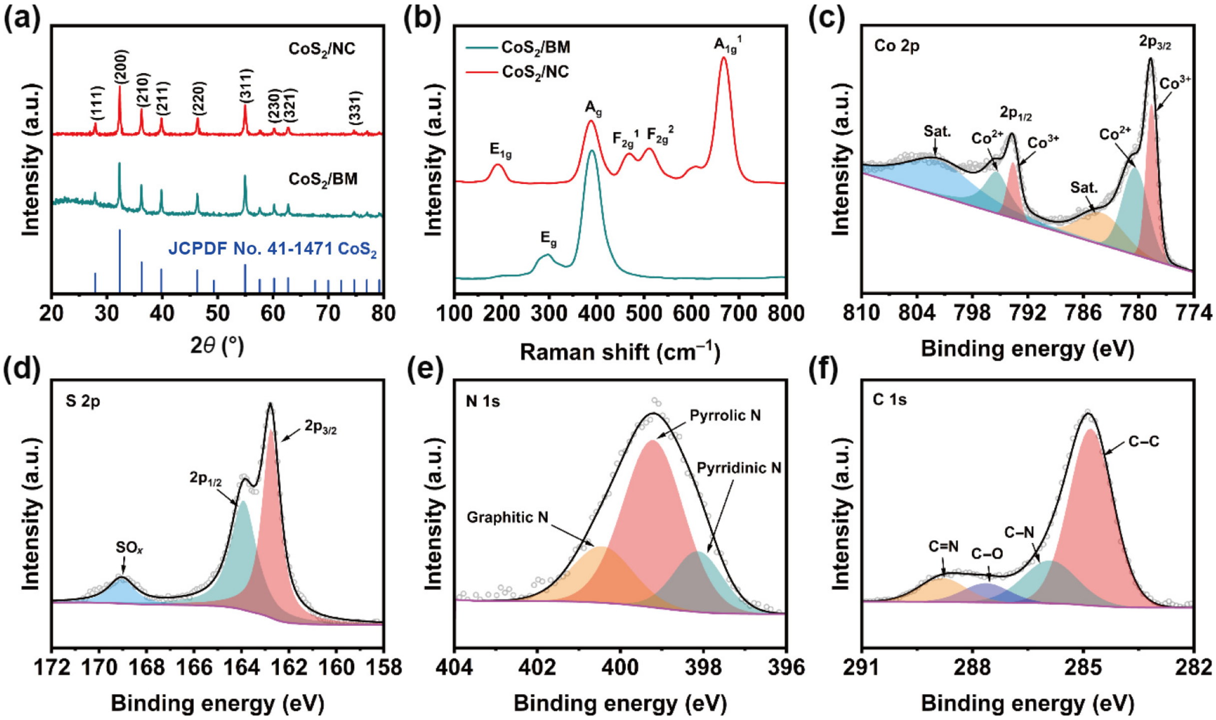

**Figure 2** (a) XRD patterns of hollow CoS$_2$/NC nanoboxes and CoS$_2$/BM. (b) Raman spectra of hollow CoS$_2$/NC nanoboxes and CoS$_2$/BM. ((c)–(f)) High-resolution XPS spectra of hollow CoS$_2$/NC nanoboxes: (c) Co 2p, (d) S 2p, (e) N 1s, and (f) C 1s.

Raman spectra in Fig. 2(b) further validated the successful synthesis, with distinct vibrational modes for both materials. The E$_{1g}$ mode, observed only in hollow CoS$_2$/NC nanoboxes, represents the opposing vibration of sulfur atoms relative to cobalt, while the A$_{1g}$ mode corresponds to symmetric sulfur displacements under compressive forces along the *c*-axis [33–38]. XRD and Raman analyses validate the successful synthesis of hollow CoS$_2$/NC nanoboxes. ICP-MS revealed that the cobalt content in hollow CoS$_2$/NC nanoboxes is 41.2 wt.%, while thermogravimetric analysis indicated that the calculated carbon content is 2.9 wt.% under ambient air conditions (Fig. S5 in the ESM) [39, 40]. Nitrogen adsorption–desorption isotherms showed Type IV isotherms with H3-type hysteresis loops, indicative of mesoporous structures (Fig. S6 in the ESM) [26, 41]. Pore size distribution analysis revealed the presence of mesopores and macropores in both materials. Hollow CoS$_2$/NC nanoboxes exhibited a specific surface area of 10.15 m$^2$·g$^{-1}$, slightly higher than the 7.10 m$^2$·g$^{-1}$ for CoS$_2$/BM.

The chemical valence states of hollow CoS$_2$/NC nanoboxes were investigated using XPS. The survey spectrum confirms the presence of Co, S, N, C, and O elements in Fig. S7 in the ESM [42]. The spectrum of Co 2p s reveals peaks corresponding to Co$^{3+}$ and Co$^{2+}$ states at 779.0/795.1 and 778.3/793.3 eV, respectively (Fig. 2(c)). Two satellite peaks at 783.7 and 801.4 eV further confirmed the coexistence of mixed oxidation states. The Co$^{2+}$ signal is primarily attributed to Co–S coordination within the CoS$_2$ crystalline structure, while the Co$^{3+}$ component is mainly due to surface oxidation [43, 44]. S 2p spectrum displays three distinct peaks at 162.8, 163.9, and 169.1 eV, corresponding to S 2p$_{2/3}$, S 2p$_{1/2}$, and oxidized sulfur species (SO$_x$), respectively (Fig. 2(d)) [34, 45, 46]. In Fig. 2(e), N 1s spectrum is deconvoluted into three states of pyridinic N (398.1 eV), pyrrolic N (399.0 eV), and graphitic N (400.4 eV) [47–49]. C 1s spectrum reveals four peaks attributed to C–C, C–N, C–O, and C=N bonds (Fig. 2(f)) [48–50].

### 3.2 Electrochemical performance

The electrochemical performance of hollow CoS$_2$/NC nanoboxes and CoS$_2$/BM was systematically evaluated using a CR2032 coin cells in Fig. 3 and Fig. S8 in the ESM. Cyclic voltammetry (CV) analysis was performed at a scan rate of 0.1 mV·s$^{-1}$. For hollow CoS$_2$/NC nanoboxes, three distinct cathodic peaks were observed in the initial cycle at 1.13, 0.81, and 0.62 V. The peaks at 1.13 and 0.81 V correspond to Na$^+$ insertion into CoS$_2$ to form Na$_x$CoS$_2$ and the simultaneous formation of a solid electrolyte interphase (SEI) film. The peak at 0.62 V is attributed to the conversion reaction to produce Na$_2$S and metallic Co from Na$_x$CoS$_2$ [18, 51]. During the anodic scan, three peaks were detected at 1.77, 1.95, and 2.00 V, corresponding to the reverse conversion reaction and Na$^+$ extraction. In subsequent cycles, the cathodic peaks shifted to 1.45, 0.93, and 0.51 V, reflecting structural reorganization after initial sodiation/desodiation process. CV curves for both hollow CoS$_2$/NC nanoboxes and CoS$_2$/BM are overlapped well after the first cycle, confirming the high reversibility (Fig. 3(a) and Fig. S8(a) in the ESM). To further elucidate the reaction mechanism of hollow CoS$_2$/NC nanoboxes, *ex-situ* XRD analysis was carried out in Fig. 3(b) and Fig. S9 in the ESM [52–54]. The dominant peaks of CoS$_2$ remained until discharge at 1.14 V, confirming the insertion of Na ions into CoS$_2$. Upon discharging to 0.81 V, the CoS$_2$-related peaks at 36.2°, 39.8°, 46.3°, and 54.9° disappeared while the peak at 32.3° remained. This corresponds to the onset of the conversion reaction, consistent with the CV results. At the same time, new peaks at 38.9°, 48.3° (Na$_2$S), 44.2°, and 51.5° (metallic Co) emerged, signifying the formation of these phases during the reaction. These peaks strengthened upon full discharge, while they weakened and eventually diminished until charged to 2.0 V. The weak CoS$_2$ (210) and (311) peaks at 36.2° and 54.9° recurred and got stronger until the end of charge process. However, other CoS$_2$-related peaks are restored with low signal due to the amorphous nature of the

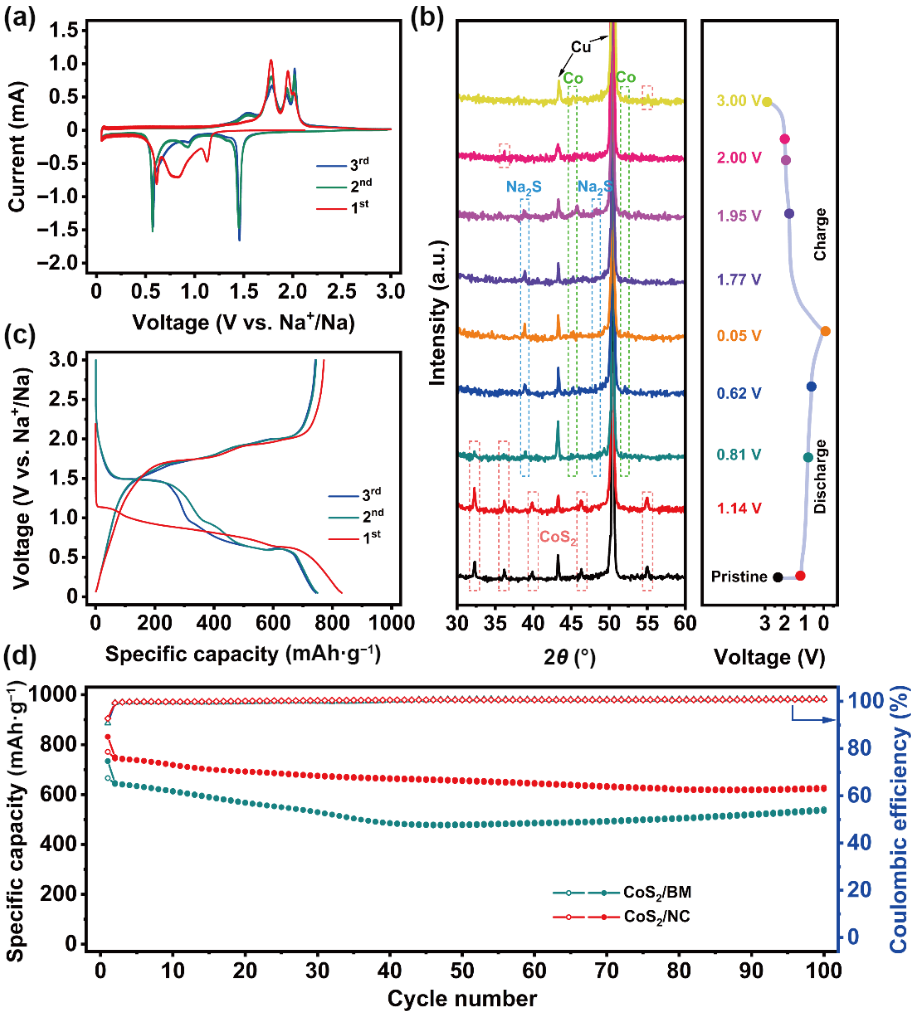

**Figure 3** (a) CV curves at 0.1 mV·s⁻¹ of hollow $CoS_2$/NC nanoboxes. (b) *Ex-situ* XRD patterns of hollow $CoS_2$/NC nanoboxes. (c) Voltage profiles at 0.5 A·g⁻¹ of hollow $CoS_2$/NC nanoboxes. (d) Cycling performance at 0.5 A·g⁻¹ of hollow $CoS_2$/NC nanoboxes and $CoS_2$/BM.

regenerated $CoS_2$. The results confirm that hollow $CoS_2$/NC nanoboxes exhibit nearly full reversibility.

As shown in Fig. 3(c) and Fig. S8(b) in the ESM, the charge/discharge profiles for the initial three cycles were presented at a voltage range of 0.05–3.00 V and a current density of 0.5 A·g⁻¹. In the first cycle, hollow $CoS_2$/NC nanoboxes exhibited sodiation and desodiation capacities of 831.3 and 771.2 mAh·g⁻¹, respectively, with an impressive initial Coulombic efficiency of 92.8%. In comparison, $CoS_2$/BM showed reversible charge capacity of 665.9 mAh·g⁻¹ with a Coulombic efficiency of 90.8%. The initial capacity loss in both materials is attributed to the SEI layer formation. From the second cycle, the voltage profiles totally overlapped for both hollow $CoS_2$/NC nanoboxes and $CoS_2$/BM, indicating the excellent stability. The cycle performance in Fig. 3(d) revealed that hollow $CoS_2$/NC nanoboxes retained a reversible capacity of 627.7 mAh·g⁻¹ after 100 cycles, significantly higher than $CoS_2$/BM (540.7 mAh·g⁻¹). The Coulombic efficiency of both materials remained close to 100%, highlighting the stability provided by the nitrogen-doped carbon matrix, which facilitates enhanced ion diffusion. The nanoboxes consisted of small $CoS_2$ nanoparticles that effectively alleviated stress and strain generated during cycling, thereby contributing to improved cycling stability.

The rate capabilities of hollow $CoS_2$/NC nanoboxes and $CoS_2$/BM are presented in Figs. 4(a) and 4(b) [55]. At various current densities of 0.5, 1, 2, 3, 5, and 10 A·g⁻¹, hollow $CoS_2$/NC nanoboxes exhibited reversible capacities of 767.5, 701.7, 654.2, 643.8, 632.2, and 607.5 mAh·g⁻¹, respectively. The performance of hollow $CoS_2$/NC nanoboxes was significantly higher than that of $CoS_2$/BM (301.4 mAh·g⁻¹), particularly at the highest current density of 10 A·g⁻¹. Upon reducing the current density back to 0.5 A·g⁻¹, both materials recovered their capacities, but the capacity of $CoS_2$/BM decreased quickly, indicating the structural advantages of the hollow nanoboxes. This is further supported by the voltage profiles for the second cycle of each current density for hollow $CoS_2$/NC nanoboxes and $CoS_2$/BM (Fig. 4(b) and Fig. S10 in the ESM). Figure 4(c) further highlights the superior rate performance of hollow $CoS_2$/NC nanoboxes compared to previously reported cobalt sulfides [9, 18, 30, 31, 56–58]. This superior performance is attributed to their unique hollow structure, composed of small nanoparticles embedded in a nitrogen-doped carbon matrix, which enhances electron conductivity and overall electrochemical properties. The long-term cycle performance at a high current density of 5 A·g⁻¹ was evaluated in Fig. 4(d). Hollow $CoS_2$/NC nanoboxes demonstrated a desodiation capacity of 618.2 mAh·g⁻¹ even after 400 cycles with cycle retention of 84.04%. The average attenuation for hollow $CoS_2$/NC nanoboxes is only 0.04% per cycle.

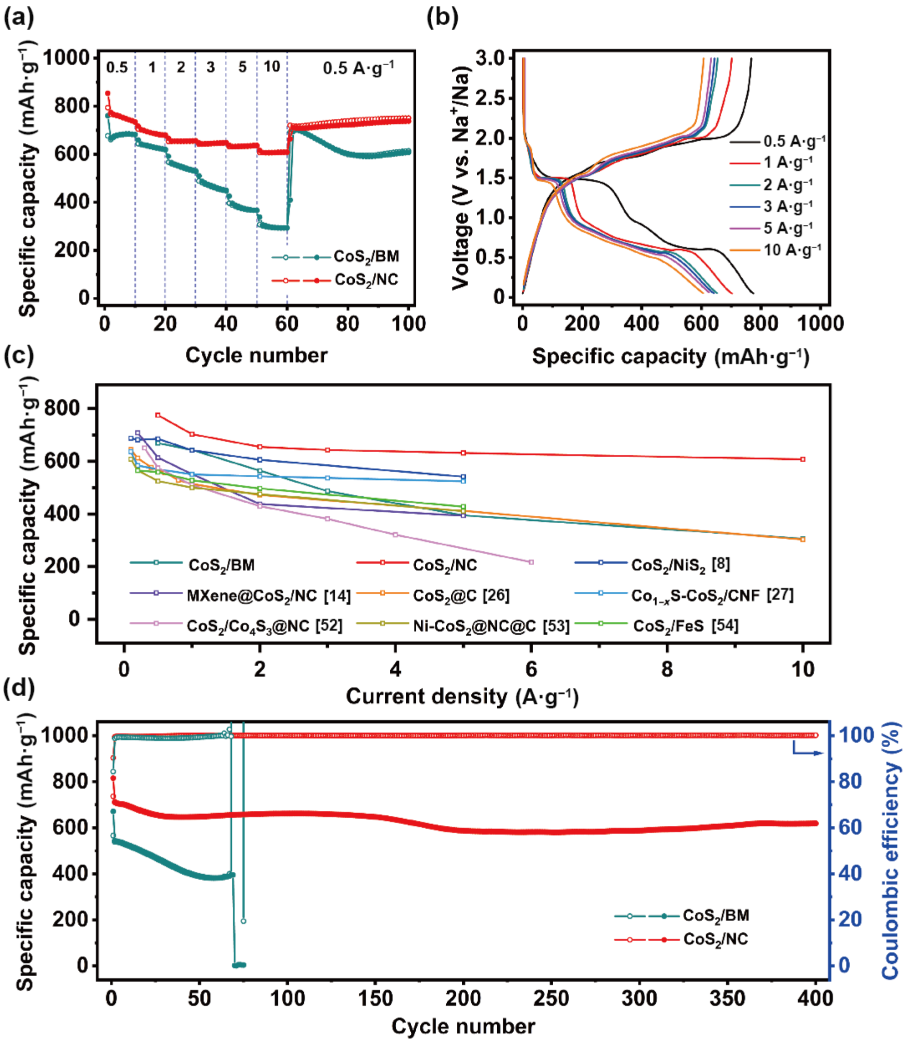

**Figure 4** (a) Rate performance of hollow $CoS_2$/NC nanoboxes and $CoS_2$/BM. (b) Voltage profiles of hollow $CoS_2$/NC nanoboxes at various current densities. (c) Comparison diagram. (d) Long-term cycle performance of hollow $CoS_2$/NC nanoboxes and $CoS_2$/BM at 5 A·g$^{-1}$.

In contrast, $CoS_2$/BM exhibited rapid degradation, failing after 69 cycles due to sodium polysulfide migration, which caused electrode corrosion and dendrite formation. These findings highlight the enhanced durability and electrochemical performance of hollow $CoS_2$/NC nanoboxes.

To further confirm the structural stability of hollow $CoS_2$/NC nanoboxes after cycling, TEM and SEM analyses were performed after 10 and 50 cycles. As illustrated in Fig. S11 in the ESM, the overall size and morphology of the nanoboxes remained almost unchanged, without significant expansion, even after 50 cycles. Notably, $CoS_2$ nanoparticles observed in Fig. S11(b) in the ESM retained a size of approximately 50 nm, validating the structural integrity of hollow $CoS_2$/NC nanoboxes derived from the Co PBAs. These observations highlight the excellent structural robustness, which enables hollow $CoS_2$/NC nanoboxes to withstand the mechanical stresses and volume changes during repeated charge–discharge processes. This structural stability ultimately contributes to the enhanced cycling performance and superior rate capability.

## 3.3 Electrochemical kinetic analysis of $CoS_2$/NC anode

To further explore the performance enhancement, the diffusion and capacitance-controlled processes of hollow $CoS_2$/NC nanoboxes and $CoS_2$/BM were analyzed. The reaction kinetics were evaluated through CV at scan rates ranging from 0.1 to 1.0 mV·s$^{-1}$ (Fig. 5(a) and Fig. S12(a) in the ESM) [32]. As the scan rate increased, the redox peak positions remained stable, while their intensity increased, indicating that the electrode does not undergo significant changes at high scan rates. The degree of capacitance contribution was determined using the power-law equation ($i = av^b$), where $i$ is the peak current, $v$ is the scan rate, and $a$ and $b$ are adjustable parameters. For hollow $CoS_2$/NC nanoboxes, the $b$-values of the five peaks were 0.69, 0.83, 0.93, 0.76, and 0.47, respectively (Fig. 5(b)). Similarly, for $CoS_2$/BM, the $b$-values were 0.59, 0.67, 0.91, 0.81, and 0.50 (Fig. S12(b) in the ESM). The peaks 1 and 5 for both electrodes showed $b$-values near 0.5, indicating a diffusion-controlled mechanism preferred during the $Na^+$ insertion and extraction. In contrast, the other peaks, related to the conversion reaction, showed $b$-values closer to 1.0, suggesting capacitance-controlled behavior. The relative contributions of diffusion- and capacitance-controlled were calculated by the equation ($i = k_1v + k_2v^{1/2}$) where $k_1v$ represents the capacitance-controlled component and $k_2v^{1/2}$ represents the diffusion-controlled component. At a scan rate of 0.1 mV·s$^{-1}$, the capacitance

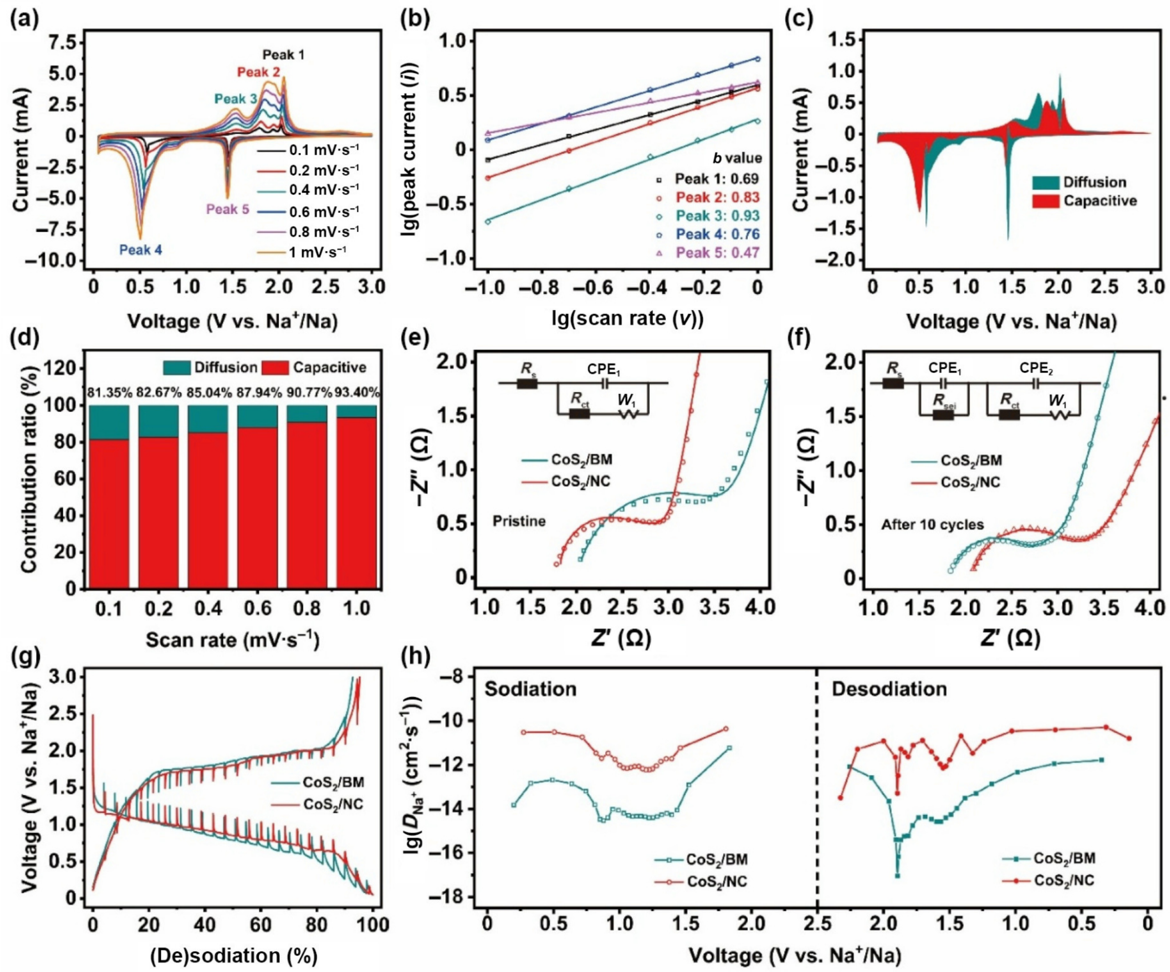

**Figure 5** (a) CV curves at different scan rates. (b) The relationship of lg($i$) and lg($v$). (c) Capacitive contribution at 0.1 mV·s$^{-1}$ of hollow $CoS_2$/NC nanoboxes. (d) Capacitive contribution ratios of hollow $CoS_2$/NC nanoboxes. ((e) and (f)) Nyquist plots of hollow $CoS_2$/NC nanoboxes and $CoS_2$/BM (e) pristine and (f) after 10 cycles. (g) GITT curves of hollow $CoS_2$/NC nanoboxes and $CoS_2$/BM. (h) Sodium ion diffusion coefficients of hollow $CoS_2$/NC nanoboxes and $CoS_2$/BM.

contribution for hollow $CoS_2$/NC nanoboxes is 81.35%, significantly higher than $CoS_2$/BM at 69.41% (Fig. 5(c) and Fig. S12(c) in the ESM). As the scan rate increased, the capacitance contribution also rose, reaching 93.40% for hollow $CoS_2$/NC nanoboxes at 1.0 mV·s$^{-1}$, compared to 88.08% for $CoS_2$/BM (Fig. 5(d) and Fig. S12(d) in the ESM). These results indicate that capacitance-controlled processes dominate at high scan rates.

EIS was performed to further investigate the reaction kinetics. As shown in the Nyquist plots (Figs. 5(e) and 5(f)), hollow $CoS_2$/NC nanoboxes exhibit a smaller semicircle compared to $CoS_2$/BM before cycling, indicating a lower charge transfer resistance ($R_{ct}$). According to the fitting results, the internal resistance ($R_s$) and $R_{ct}$ of hollow $CoS_2$/NC nanoboxes were 1.84 and 0.67 Ω, respectively, while those for $CoS_2$/BM were 2.00 and 1.85 Ω [59]. After 10 cycles, $R_{ct}$ of hollow $CoS_2$/NC nanoboxes significantly decreased to 0.005 Ω, much lower than $CoS_2$/BM (0.2 Ω). This significant reduction is attributed to the activation process during cycling. These results highlight the superior $Na^+$ diffusion kinetics of hollow $CoS_2$/NC nanoboxes, which play a key role in their enhanced electrochemical performance. The $Na^+$ diffusion coefficient during the sodiation/desodiation process was calculated using the galvanostatic intermittent titration technique (GITT) at 0.1 A·g$^{-1}$ (Figs. 5(g) and 5(g)) [60–62]. Hollow $CoS_2$/NC nanoboxes show a diffusion coefficient ($10^{-11}$–$10^{-14}$ cm$^2$·s$^{-1}$), which is 2–4 orders of magnitude higher than that of $CoS_2$/BM. This significant improvement in $Na^+$ diffusion confirms the positive impact of incorporating a nitrogen-doped carbon matrix on both electronic conductivity and ionic diffusion. This enhancement can also be confirmed by electrical conductivity measurements. According to the four-point probe results, the electrical conductivity of hollow $CoS_2$/NC nanoboxes is $5.11 \times 10^{-1}$ S·cm$^{-1}$, significantly higher than that of $CoS_2$/BM ($7.65 \times 10^{-4}$ S·cm$^{-1}$). This nearly 3 order of magnitude increase highlights the superior electrical conductivity of the hollow $CoS_2$/NC nanoboxes derived from Co PBAs. The substantial improvement in both $Na^+$ diffusion and electrical conductivity underscores the beneficial role of the nitrogen-doped carbon matrix and the hollow structure in enhancing electronic conductivity and facilitating ion transport.

## 4 Conclusions

In summary, Co PBAs were synthesized via a self-assembly method, followed by sulfidation to produce hollow $CoS_2$/NC nanoboxes composed of 50 nm $CoS_2$ nanoparticles. This unique hollow structure, combined with the incorporation of a nitrogen-doped carbon matrix, significantly enhanced the electrochemical performance in SIBs. Hollow $CoS_2$/NC nanoboxes exhibited a high reversible capacity of 771.2 mAh·g$^{-1}$ at 0.5 A·g$^{-1}$, an initial

Coulombic efficiency of 92.8%, excellent capacity retention at high current density (607.5 mAh·g$^{-1}$ at 10 A·g$^{-1}$), and remarkable long cycle stability over 400 cycles at 5 A·g$^{-1}$, with an average capacity decay of only 0.04% per cycle. Kinetic analysis revealed that the capacitive-controlled process was the dominant mechanism, while the nitrogen-doped carbon matrix facilitated improved Na$^+$ diffusion, contributing to the enhanced electrochemical performance. This study provides a straightforward approach for synthesizing nanoscale metal sulfides with a nitrogen-doped carbon matrix, offering a promising pathway to develop SIB electrodes with extended cycle life and high capacity.

**Electronic Supplementary Material**: Supplementary material (SEM, TEM, XRD, TGA, BET, XPS, and electrochemical performance results) is available in the online version of this article at https://doi.org/10.26599/NR.2025.94907800.

## Data availability

All data needed to support the conclusions in the paper are presented in the manuscript and the Electronic Supplementary Material. Additional data related to this paper may be requested from the corresponding author upon request.

## Acknowledgements

This work was financially supported by the Jilin Provincial Education Department (No. JJKH20230615KJ), National Research Foundation of Korea (NRF) grant funded by the Korea Government (MSIT, No. NRF-RS-2024-00446785), the Science and Technology Development Plan Project of Jilin Province, China (No. YDZJ202401373ZYTS), and the Higher Education Discipline Innovation Project (No. D18012).

## Declaration of competing interest

All the contributing authors report no conflict of interests in this work.

## Author contribution statement

S. J. X.: Data curation, project administration, validation, experimental design, writing – original draft, writing – review & editing. N. L.: Data curation, validation, experimental design. H. K.: Data curation, experimental design. W. S. B.: Data curation, investigation. S. H. K.: Data curation, investigation. A. H. J.: Project administration, funding acquisition, writing – review & editing. S.-H. Y.: Project administration, funding acquisition. B. Q.: Project administration, funding acquisition. All the authors have approved the final manuscript.

## Use of AI statement

None.

## References

[1] Jiang, M. W.; Ren, L. B.; Hou, Z. D.; Hua, W.; Lei, D.; Cao, Y. J.; Zhang, Y.; Wang, J. G. A superior sodium-ion battery based on tubular Prussian blue cathode and its derived phosphide anode. *J. Power Sources* **2023**, *554*, 232334.

[2] Cheng, Q.; Deng, Q.; Zhong, W. T.; Tan, T.; Liu, X. Z.; Chen, C. D.; Hu, J. H.; Lin, Z.; Huang, K.; Yang, C. H. Criticality of solid electrolyte interphase in achieving high performance of sodium-ion batteries. *Chem. Eng. J.* **2023**, *457*, 141097.

[3] Huang, X. F.; Tao, K. H.; Han, T. L.; Li, J. J.; Zhang, H. G.; Hu, C. Q.; Niu, J. J.; Liu, J. Y. Long-cycling-life sodium-ion battery using binary metal sulfide hybrid nanocages as anode. *Small* **2023**, *19*, 2302706.

[4] Chen, J. W.; Chua, D. H. C.; Lee, P. S. The advances of metal sulfides and *in situ* characterization methods beyond Li ion batteries: Sodium, potassium, and aluminum ion batteries. *Small Methods* **2020**, *4*, 1900648.

[5] Yu, G.; Hu, Y. F., H.; Wang, W. W.; You, E. M.; Tang, S.; Su, J. J.; Yi, J.; Yan, J. W.; Tian, Z. Q.; Mao, B. W. An *in-situ* Raman spectroscopic study on the interfacial process of carbonate-based electrolyte on nanostructured silver electrode. *J. Electrochem.* **2023**, *29*, 2301261.

[6] Armand, M.; Tarascon, J. M. Building better batteries. *Nature* **2008**, *451*, 652–657.

[7] Dunn, B.; Kamath, H.; Tarascon, J. M. Electrical energy storage for the grid: A battery of choices. *Science* **2011**, *334*, 928–935.

[8] Abakumov, A. M.; Fedotov, S. S.; Antipov, E. V.; Tarascon, J. M. Solid state chemistry for developing better metal-ion batteries. *Nat. Commun.* **2020**, *11*, 4976.

[9] Wang, J. J.; Yue, X. Y.; Cao, X.; Liu, Z.; Patil, A. M.; Wang, J. W.; Hao, X. G.; Abudula, A.; Guan, G. Q. Metal organic frameworks derived CoS$_2$/NiS$_2$ heterostructure toward high-performance sodium storage anode materials. *Chem. Eng. J.* **2022**, *431*, 134091.

[10] Fu, Y. C.; Sun, J.; Zhang, Y. S.; Qu, W.; Wang, W. C.; Yao, M.; Zhang, Y.; Wang, Q.; Tang, Y. F. Revealing Na$^+$-coordination induced failure mechanism of metal sulfide anode for sodium ion batteries. *Angew. Chem., Int. Ed.* **2024**, *63*, e202403463.

[11] Li, T.; Wang, B. X.; Song, H. B.; Mei, P.; Hu, J. P.; Zhang, M. M.; Chen, G. H.; Yan, D.; Zhang, D. H.; Huang, S. Z. Deciphering the performance enhancement, cell failure mechanism, and amelioration strategy of sodium storage in metal chalcogenides-based anodes. *Adv. Mater.* **2024**, *36*, 2314271.

[12] Geng, P. B.; Zheng, S. S.; Tang, H.; Zhu, R. M.; Zhang, L.; Cao, S.; Xue, H. G.; Pang, H. Transition metal sulfides based on graphene for electrochemical energy storage. *Adv. Energy Mater.* **2018**, *8*, 1703259.

[13] Liu, J.; Lou, C. J.; Fu, J. P.; Sun, X.; Hou, J. R.; Ma, J. W.; Chen, Y. J.; Gao, X.; Xu, L. G.; Wei, Q. et al. Multiple transition metals modulated hierarchical networks for high performance of metal-ion batteries. *J. Energy Chem.* **2022**, *70*, 604–613.

[14] You, S. Z.; Deng, Q.; Zhang, Q. M.; Huang, K.; Yang, C. H. Mechanistic insights into the interactions between a new type of hard carbon anode and organic electrolytes in sodium-ion batteries. *ACS Sustain. Chem. Eng.* **2023**, *11*, 10590–10597.

[15] Yang, C. Y.; Zhong, W. T.; Liu, Y. Q.; Deng, Q.; Cheng, Q.; Liu, X. Z.; Yang, C. H. Regulating solid electrolyte interphase film on fluorine-doped hard carbon anode for sodium-ion battery. *Carbon Energy* **2024**, *6*, e503.

[16] You, S. Z.; Zhang, Q. B.; Liu, J. X.; Deng, Q.; Sun, Z. F.; Cao, D. D.; Liu, T. C.; Amine, K.; Yang, C. H. Hard carbon with an opened pore structure for enhanced sodium storage performance. *Energy Environ. Sci.* **2024**, *17*, 8189–8197.

[17] Li, X. T.; Liang, H. J.; Liu, X. L.; Sun, R.; Qin, Z. X.; Fan, H. S.; Zhang, Y. F. Ion-exchange strategy of CoS$_2$/Sb$_2$S$_3$ hetero-structured nanocrystals encapsulated into 3D interpenetrating dual-carbon framework for high-performance Na$^+$/K$^+$ batteries. *Chem. Eng. J.* **2021**, *425*, 130657.

[18] Li, Q.; Jiao, Q. Z.; Yan, Y.; Li, H. J.; Zhou, W.; Gu, T. T.; Shen, X. R.; Lu, C. X.; Zhao, Y.; Zhang, Y. Y. et al. Optimized Co–S bonds energy and confinement effect of hollow MXene@CoS$_2$/NC for enhanced sodium storage kinetics and stability. *Chem. Eng. J.* **2022**, *450*, 137922.

[19] Wang, R. H.; Qian, C. F.; Zhang, Z. R.; Shen, H.; Xia, J. J.; Cui, D.

Y.; Sun, K. W.; Liu, H.; Guo, C.; Yu, F. et al. Advance of Prussian blue-derived nanohybrids in energy storage: Current status and perspective. *Small* **2023**, *19*, 2206848.

[20] Ma, F.; Li, Q.; Wang, T. Y.; Zhang, H. G.; Wu, G. Energy storage materials derived from Prussian blue analogues. *Sci. Bull.* **2017**, *62*, 358–368.

[21] Shen, M. H.; Ma, H. L. Metal–organic frameworks (MOFs) and their derivative as electrode materials for lithium-ion batteries. *Coord. Chem. Rev.* **2022**, *470*, 214715.

[22] Shang, Z. X.; Chen, Z. L.; Zhang, Z. B.; Yu, J.; Tan, S. Z.; Ciucci, F.; Shao, Z. P.; Lei, H.; Chen, D. J. CoFe nanoalloy particles encapsulated in nitrogen-doped carbon layers as bifunctional oxygen catalyst derived from a Prussian blue analogue. *J. Alloys Compd.* **2018**, *740*, 743–753.

[23] Chang, X. W.; Liu, T. T.; Li, W. L.; Gao, R. X.; Lei, H.; Ren, Z. Y. Porous Prussian blue analogs derived nickel-iron bimetallic phosphide nanocubes on conductive hollow mesoporous carbon nanospheres for stable and flexible high-performance supercapacitor electrode. *J. Colloid Interface Sci.* **2023**, *650*, 728–741.

[24] Chen, J. W.; Li, S. H.; Kumar, V.; Lee, P. S. Carbon coated bimetallic sulfide hollow nanocubes as advanced sodium ion battery anode. *Adv. Energy Mater.* **2017**, *7*, 1700180.

[25] Je, J.; Lim, H.; Jung, H. W.; Kim, S. O. Ultrafast and ultrastable heteroarchitectured porous nanocube anode composed of CuS/$FeS_2$ embedded in nitrogen-doped carbon for use in sodium-ion batteries. *Small* **2021**, *18*, 2105310.

[26] Chen, S. M.; Ma, L. T.; Wu, S. L.; Wang, S. Y.; Li, Z. B.; Emmanuel, A. A.; Huqe, M. R.; Zhi, C. Y.; Zapien, J. A. Uniform virus-like Co–N–Cs electrocatalyst derived from Prussian blue analog for stretchable fiber-shaped Zn–air batteries. *Adv. Funct. Mater.* **2020**, *30*, 1908945.

[27] Huang, Y.; Zhang, X.; Ji, L.; Wang, L.; Xu, B. B.; Shahzad, M. W.; Tang, Y. X.; Zhu, Y. F.; Yan, M.; Sun, G. X. et al. Boosting the sodium storage performance of Prussian blue analogs by single-crystal and high-entropy approach. *Energy Storage Mater.* **2023**, *58*, 1–8.

[28] Wang, X.; Lu, J. Y.; Han, W. J.; Yang, J. Q.; Jiang, B.; Sun, Y. F.; Zhang, H.; Lu, G. Y. Co–PBA MOF-derived hierarchical hollow $Co_3O_4$@NiO microcubes functionalized with Pt for superior $H_2S$ sensing. *Sens. Actuators B: Chem.* **2021**, *342*, 130028.

[29] Wu, W. T.; Wu, Y. F.; Zhang, Z. Q.; Sun, L. P.; Wei, R. P.; Zhang, J.; Gao, L. J.; Pan, X. M.; Yu, J.; Xiao, G. M. Multichannel electron transmission and multiple light scattering in CoCo PBA/$CoSn(OH)_6$/Pt photocatalyst for effective conversion of simulated flue gas. *Fuel* **2023**, *334*, 126747.

[30] Zhao, Z. P.; Li, S. H.; Li, C. Q.; Liu, Z. Y.; Li, D. Hollow $CoS_2$@C nanocubes for high-performance sodium storage. *Appl. Surf. Sci.* **2020**, *519*, 146268.

[31] Chen, D. M.; Wu, Y. C.; Huang, Z. Q.; Wang, K. H.; Zhu, X.; Wang, Z.; Chen, J. Phase transformation controlled $Co_{1-x}S$–$CoS_2$ heterostructures embedded in S-doped carbon nanofibers for superior sodium-ion storage. *Chem. Eng. J.* **2023**, *457*, 141181.

[32] Yin, X. C.; Liu, Y. J.; Ren, Y.; Zhou, Y. L.; Cheng, X. Q.; Chen, M.; Du, C. Y.; Yin, G. P.; Huo, H. Chemical/electrochemical dual-driven transition behavior of copper element from current collector to chalcogenide anode in sodium-ion batteries. *Adv. Funct. Mater.* **2024**, *34*, 2312841.

[33] Ma, D.; Hu, B.; Wu, W. D.; Liu, X.; Zai, J. T.; Shu, C.; Tadesse Tsega, T.; Chen, L. W.; Qian, X. F.; Liu, T. L. Highly active nanostructured $CoS_2$/CoS heterojunction electrocatalysts for aqueous polysulfide/iodide redox flow batteries. *Nat. Commun.* **2019**, *10*, 3367.

[34] Wen, X.; Feng, W.; Li, X. H.; Yang, J. B.; Du, R. F.; Wang, P.; Li, H.; Song, L. Y.; Wang, Y. Z.; Cheng, M. et al. Diatomite-templated synthesis of single-atom cobalt-doped $MoS_2$/carbon composites to boost sodium storage. *Adv. Mater.* **2023**, *35*, 2211690.

[35] Lv, Z. R.; Zhao, C. D.; Xie, M.; Cai, M. Z.; Peng, B. X.; Ren, D. Y.; Fang, Y. Q.; Dong, W. J.; Zhao, W.; Lin, T. Q. et al. 1D insertion chains induced small-polaron collapse in $MoS_2$ 2D layers toward fast-charging sodium-ion batteries. *Adv. Mater.* **2024**, *36*, 2309637.

[36] Li, E. Z.; Wang, M. S.; Hu, X.; Huang, S. M.; Yang, Z. L.; Chen, J. C.; Yu, B.; Guo, B. S.; Ma, Z. Y.; Huang, Y. et al. $NH_4^+$ pre-intercalation and Mo doping $VS_2$ to regulate nanostructure and electronic properties for high efficiency sodium storage. *Small* **2024**, *20*, 2308630.

[37] Zhang, G. X.; Chen, X. R.; Yu, X. M.; Li, Q. Y.; Wang, H. Q.; Hu, S. J.; Jiang, J. T.; Huang, Y. G.; Ma, Z. L. Crystalline–amorphous heterostructure on the phosphatized P–$CoS_2$/CNT for augmenting the catalytic conversion kinetics of Li–S batteries. *Chem. Eng. J.* **2024**, *488*, 150696.

[38] Agboola, P. O.; Shakir, I.; Almutairi, Z. A.; Shar, S. S.; Aboud, M. F. A. Carbon nanotubes fabricated $Mn^{+2}$ doped $CoS_2$ composite-decorated on nickel foam as hybrid electrode material for supercapacitor applications. *Phys. B: Condens. Matter.* **2022**, *644*, 414211.

[39] Jing, M. J.; Chen, Z. G.; Li, Z.; Li, F. Y.; Chen, M. J.; Zhou, M. J.; He, B. H.; Chen, L.; Hou, Z. H.; Chen, X. B. Facile synthesis of ZnS/N,S Co-doped carbon composite from zinc metal complex for high-performance sodium-ion batteries. *ACS Appl. Mater. Interfaces* **2017**, *10*, 704–712.

[40] Jiang, M. W.; Hou, Z. D.; Wang, J. J.; Ren, L. B.; Zhang, Y.; Wang, J. G. Balanced coordination enables low-defect Prussian blue for superfast and ultrastable sodium energy storage. *Nano Energy* **2022**, *102*, 107708.

[41] Li, J. B.; Yan, D.; Zhang, X. J.; Hou, S. J.; Lu, T.; Yao, Y. F.; Pan, L. K. ZnS nanoparticles decorated on nitrogen-doped porous carbon polyhedra: A promising anode material for lithium-ion and sodium-ion batteries. *J. Mater. Chem. A* **2017**, *5*, 20428–20438.

[42] Shi, X. D.; Xu, Z. M.; Han, C.; Shi, R. Z.; Wu, X. W.; Lu, B. A.; Zhou, J.; Liang, S. Q. Highly dispersed cobalt nanoparticles embedded in nitrogen-doped graphitized carbon for fast and durable potassium storage. *Nano-Micro Lett.* **2021**, *13*, 21.

[43] Kang, X. Y.; Dong, Y. T.; Guan, H.; Al-Tahan, M. A.; Zhang, J. M. Manipulating the electrocatalytic activity of sulfur cathode via distinct cobalt sulfides as sulfur host materials in lithium–sulfur batteries. *J. Colloid Interface Sci.* **2022**, *622*, 515–525.

[44] Li, Y. H.; Zhang, Q. F.; Song, Z. T.; Shu, K.; Yang, Z. Z.; Hu, H. M.; Lu, Y.; Tang, X.; Zhou, X. J. Manipulating the morphology and the electronic structures of nickel-cobalt selenides@N-doped carbon for aqueous alkaline batteries. *Colloids Surf. A: Physicochem. Eng. Aspects* **2022**, *655*, 130191.

[45] Hu, J. J.; Liu, C.; Cai, C.; Sun, Q. Q.; Lu, M. X.; Yao, Z. J.; Yang, Y. F. Prussian blue analogue-derived Fe-doped $CoS_2$ nanoparticles confined in bayberry-like N-doped carbon spheres as anodes for sodium-ion batteries. *Polymers* **2023**, *15*, 1496.

[46] Wang, F.; Han, F.; He, Y. L.; Zhang, J.; Wu, H.; Tao, J.; Zhang, C. Z.; Zhang, F. Q.; Liu, J. S. Unraveling the voltage failure mechanism in metal sulfide anodes for sodium storage and improving their long cycle life by sulfur-doped carbon protection. *Adv. Funct. Mater.* **2021**, *31*, 2007266.

[47] Zhang, H. Y.; Cui, H. T.; Li, J.; Liu, Y. Y.; Yang, Y. Z.; Wang, M. R. Frogspawn inspired hollow $Fe_3C$@N–C as an efficient sulfur host for high-rate lithium–sulfur batteries. *Nanoscale* **2019**, *11*, 21532–21541.

[48] Dong, X. Y.; Wang, J. X.; Wang, X.; Xu, J. Y.; Yang, J. D.; Zeng, W.; Li, Y. H.; Zhao, Y. F.; Huang, G. S.; Wang, J. F.; Pan, F. S. Bimetallic CuCo@nitrogen/carbon nanoparticles as a cathode catalyst for magnesium–air batteries. *ChemElectroChem* **2022**, *9*, e202200585.

[49] Song, J.; Li, Y. X.; Lu, X. M.; Zhang, W.; Xiang, Y. X.; Chen, J. Z.; Tian, Q. H. Converting Prussian blue to porous cubic $Fe_3O_4$/nitrogen-doped carbon nanocomposite through a space-confined calcination

strategy for high lithium storage anodes. *Appl. Surf. Sci.* **2022**, *604*, 154502.

[50] Wang, J.; Yin, H. H.; Xu, Y. T.; Chen, Z.; Gao, J. F.; Wang, Z. Q.; Zuo, S. L. Pyrolysis of Prussian blue for lignin-derived nitrogen-doped biocarbon to boost sodium storage. *Ind. Crops. Prod.* **2023**, *192*, 116079.

[51] Xiao, F. P.; Yang, X. M.; Wang, D. H.; Wang, H. M.; Yu, D. Y. W.; Rogach, A. L. Metal–organic framework derived $CoS_2$ wrapped with nitrogen-doped carbon for enhanced lithium/sodium storage performance. *ACS Appl. Mater.* **2020**, *12*, 12809–12820.

[52] Kim, S. Y.; Ahn, H. J.; Kim, Y. H.; Kim, H. K.; Lee, B. H.; Byeon, Y. W.; Park, J. H.; Chung, K. Y.; Lee, J. C. Self-assembling CuS anodes with conversion reaction for ultrafast Na-ion storage. *J. Mater. Chem. A* **2023**, *11*, 21972–21982.

[53] Yang, M. M.; Kong, Q. Q.; Feng, W.; Yao, W. T. N/O double-doped biomass hard carbon material realizes fast and stable potassium ion storage. *Carbon* **2021**, *176*, 71–82.

[54] Li, J. B.; Yan, D.; Lu, T.; Yao, Y. F.; Pan, L. K. An advanced CoSe embedded within porous carbon polyhedra hybrid for high performance lithium-ion and sodium-ion batteries. *Chem. Eng. J.* **2017**, *325*, 14–24.

[55] Guo, Z. Y.; Xu, Z.; Xie, F.; Jiang, J. L.; Zheng, K. T.; Alabidun, S.; Crespo-Ribadeneyra, M.; Hu, Y. S.; Au, H.; Titirici, M. M. Investigating the superior performance of hard carbon anodes in sodium-ion compared with lithium- and potassium-ion batteries. *Adv. Mater.* **2023**, *35*, 2304091.

[56] Dong, C. F.; Guo, L. J.; Li, H. B.; Zhang, B.; Gao, X.; Tian, F.; Qian, Y. T.; Wang, D. B.; Xu, L. Q. Rational fabrication of $CoS_2/Co_4S_3$@N-doped carbon microspheres as excellent cycling performance anode for half/full sodium ion batteries. *Energy Storage Mater.* **2020**, *25*, 679–686.

[57] Li, Q. P.; Wang, P.; Chen, Y. X.; Liao, X. Y.; Lam, K. H.; Zhang, H.; Zheng, Q. J.; Lin, D. M. Rod-like Ni–$CoS_2$@NC@C: Structural design, heteroatom doping and carbon confinement engineering to synergistically boost sodium storage performance. *J. Colloid Interface Sci.* **2024**, *664*, 400–408.

[58] Lu, M. X.; Liu, C.; Sun, Q. Q.; Ren, G. Y.; Li, Y. X.; Wang, Y. T.; Gao, J. Y.; Yao, Z. J.; Yang, Y. F. Ion-exchange route induced heterostructured $CoS_2$/FeS nanoparticles confined in hollow N-doped carbon frameworks for enhanced sodium storage performance. *ACS Appl. Nano Mater.,* **2023**, *6*, 11944–11954.

[59] Dutta, D. P.; Pathak, D. D.; Abraham, S.; Ravuri, B. R. An insight into the sodium-ion and lithium-ion storage properties of CuS/graphitic carbon nitride nanocomposite. *RSC Adv.* **2022**, *12*, 12383–12395.

[60] Feng, J.; Luo, S. H.; Yan, S. X.; Zhan, Y.; Wang, Q.; Zhang, Y. H.; Liu, X.; Chang, L. J. Hierarchically nitrogen-doped carbon wrapped $Ni_{0.6}Fe_{0.4}Se_2$ binary-metal selenide nanocubes with extraordinary rate performance and high pseudocapacitive contribution for sodium-ion anodes. *J. Mater. Chem. A* **2021**, *9*, 1610–1622.

[61] Zheng, T.; Hu, P. F.; Wang, Z. C.; Guo, T. Q. 2D amorphous iron selenide sulfide nanosheets for stable and rapid sodium-ion storage. *Adv. Mater.* **2023**, *35*, 2306577.

[62] Guo, M. Y.; Zhang, H.; Huang, Z.; Li, W. B.; Zhang, D. Y.; Gao, C. Q.; Gao, F.; He, P.; Wang, J. G.; Chen, W. H. et al. Liquid template assisted activation for “egg puff”-like hard carbon toward high sodium storage performance. *Small* **2023**, *19*, 2302583.